*membranes*

MDPI

*Article*

# Mixed-Matrix Organo-Silica–Hydrotalcite Membrane for $CO_2$ Separation Part 1: Synthesis and Analytical Description

**Lucas Bünger *, Krassimir Garbev *, Angela Ullrich, Peter Stemmermann and Dieter Stapf**

Institute for Technical Chemistry, Karlsruhe Institute of Technology, 76344 Karlsruhe, Germany; angela.ullrich@kit.edu (A.U.); peter.stemmermann@kit.edu (P.S.); dieter.stapf@kit.edu (D.S.)

* Correspondence: lucas.buenger@kit.edu (L.B.); krassimir.garbev@kit.edu (K.G.); Tel.: +49-721-6082-4405 (L.B.); +49-721-6082-6878 (K.G.)

**Abstract:** Hydrotalcite exhibits the capability to adsorb $CO_2$ at elevated temperatures. High surface area and favorable coating properties are essential to harness its potential for practical applications. Stable alcohol-based dispersions are needed for thin film applications of mixed membranes containing hydrotalcite. Currently, producing such dispersions without the need for delamination and dispersing agents is a challenging task. This work introduces, for the first time, a manufacturing approach to overcoming the drawbacks mentioned above. It includes a synthesis of hydrotalcite nanoparticles, followed by agent-free delamination of their layers and final dispersion into alcohol without dispersing agents. Further, the hydrotalcite-derived sorption agent is dispersed in a matrix based on organo-silica gels derived from 1,2-bis(triethoxysilyl)ethane (BTESE). The analytical results indicate that the interconnection between hydrotalcite and BTESE-derived gel occurs via forming a strong hydrogen bonding system between the interlayer species (OH groups, $CO_3^{2-}$) of hydrotalcite and oxygen and silanol active gel centers. These findings lay the foundation for applications involving incorporating hydrotalcite-like compounds into silica matrices, ultimately enabling the development of materials with exceptional mass transfer properties. In part 2 of this study, the gas separation performance of the organo-silica and the hydrotalcite-like materials and their combined form will be investigated.

**Keywords:** hydrotalcite; BTESE gel; delamination; $CO_2$ separation; mixed-matrix membrane

check for updates

**Citation:** Bünger, L.; Garbev, K.; Ullrich, A.; Stemmermann, P.; Stapf, D. Mixed-Matrix Organo-Silica–Hydrotalcite Membrane for $CO_2$ Separation Part 1: Synthesis and Analytical Description. *Membranes* **2024**, *14*, 170. https://doi.org/10.3390/membranes14080170

Academic Editors: Naiying Du and Haiqing Lin

Received: 31 May 2024
Revised: 29 July 2024
Accepted: 5 August 2024
Published: 6 August 2024

**Copyright:** © 2024 by the authors. Licensee MDPI, Basel, Switzerland. This article is an open access article distributed under the terms and conditions of the Creative Commons Attribution (CC BY) license (https://creativecommons.org/licenses/by/4.0/).

## 1. Introduction

Gas separation processes play an important part in reaching carbon-neutral production. Especially high-temperature applications that depend on suitable materials that can efficiently capture $CO_2$ above 200 °C receive more attention [1]. Fortunately, sorbent research has made tremendous efforts in the past to investigate the adsorption properties of inorganic materials such as Hydrotalcite-like compounds (HTlcs).

The mineral hydrotalcite, $[Mg_6Al_2(OH)_{16}](CO_3)(H_2O)_4$, was first described in 1842 by Hochstetter in serpentine–magnesite rocks in Snarum, Buskerud, Norway [2]. It belongs to the hydrotalcite supergroup of minerals, also known as layered double hydroxides (LDHs). More than 40 structurally and chemically related varieties are known so far [3]. All LDH crystal structures share the similarity of being built up of positively charged brucite-type layers. Their octahedral sites are mainly occupied by $M^{2+}$ and $M^{3+}$ cations, where $M^{2+}$ are Mg, Fe, Mn, Ni, Cu, Ca, and Zn, whereas $M^{3+}$ are Al, Fe, Mn, Co, and Cr. The octahedral layers alternate with negatively charged interlayers occupied by $(CO_3)^{2-}$, $H_2O$, $Cl^-$, etc. The crystal structures of hydrotalcite-like compounds and their polytypes have been the object of numerous studies: Allmann and Jepsen (1969) [4] and Bellotto et al. (1996) [5] for the variety quintinite ($M^{2+}/M^{3+} = 2$) and Zhitova et al. (2019) for the "true" hydrotalcite ($M^{2+}/M^{3+} = 3$) [6].

Synthetic materials on an LDH basis are in great demand due to their useful physicochemical properties [7]. Their ability to function as a high-temperature adsorption agent for

$CO_2$ has been studied extensively [8–11]. However, the bulk of these investigations focuses on HTlc materials in their layered and powdery forms rather than technical applications. To bridge this gap and realize their potential in real-world applications, a transformation of HTlc is essential. The preferred approach involves converting them into a delaminated state, which offers an enlarged surface area for more effective interactions [12]. Delaminated HTlcs have a broad range of applications, including their use as catalysts [13], enhanced drug delivery [14], biosensors, and adsorbents [15]. Their use as pure material membranes has not shown convincing results due to the resulting porosity that facilitates only Knudsen diffusion [16,17]. However, their utilization as adsorptive mass transfer agents in polymeric membranes has already demonstrated efficacy at lower temperatures [18].

For high-temperature membrane applications, a mixed-matrix approach seems to be promising. Attempts to incorporate hydrotalcite-derived substances in water-based γ-alumina matrices yielded mesoporous microstructures with unselective Knudsen diffusion [19]. Amorphous organo-silica has proven to be a suitable material as it forms a microporous microstructure that enables selective mass transport and withstands harsh process conditions [20–23]. These silica matrices are prepared from alcohol-based dispersions, which are highly sensitive to water. In the preparation of the mixed-matrix membrane, the hydrotalcite-derived adsorption agent must, therefore, be in a stable alcohol-based form, completely devoid of water content, while possessing similar drying characteristics to the matrix. Gels derived from 1,2-bis(triethoxysilyl)ethane (BTESE) are considered suitable matrices as their linking units could be used to control the membrane pore sizes. However, these membranes experience a loss of selectivity at higher temperatures due to a decrease in adsorptive affinity for $CO_2$ [24,25] and an increase in $N_2$ permeance caused by activated permeation [26–28]. An excellent review of the state of the scientific knowledge and technology regarding the application of organo-silica membranes for gas separation purposes is given by I. Agirre et al. [29]. The high-temperature adsorption agent HTlc combined with a microporous organo-silica xerogel matrix is envisioned to offset their respective weaknesses.

The use of delaminating and dispersing agents presents challenges as they tend to persist on the substance post-drying. While these agents can be eliminated during thermal treatment, they create porosity, thereby compromising the selectivity of the resulting membrane for gas separation applications.

Successful delamination processes using formamide as a solvent have shown promising results; however, there is an effort to find alternatives due to its toxicity. Recent research suggests positive outcomes with a combination of dodecyl sulfate and n-butanol as an alcoholic dispersant [30]. Additionally, experiments with sodium acetate have demonstrated stable HTlc dispersions in ethanol [31]. However, all these processes combine the disadvantage of either utilizing large amounts of dispersing agents, a solvent with different drying properties than ethanol, or the HTlc not being in its active $CO_2$ adsorptive form. The synthesis of the precursor for the $CO_2$ adsorbing compound, hydrotalcite, offers various routes described in the literature [32]. However, for the specific application of creating stable ethanol-based dispersions, the focus lies particularly on preparing particles of a nanometer size.

Therefore, this study shows an approach to creating an HTlc-derived adsorption agent in ethanol without the use of a dispersing agent. Firstly, the preparation method of the hydrotalcite is presented, then its delamination in water, and finally, the transformation of the calcined active form into the ready-for-use ethanol dispersion. Furthermore, the combination of the produced dispersion is investigated after mixing it with the aforementioned silica matrix based on BTESE gel derivates. All described steps are analyzed using various techniques to determine their respective composition and structural properties and how they vary during processing.

## 2. Materials and Methods

### *2.1. Preparation*

#### 2.1.1. Hydrotalcite

The synthesis of hydrotalcite is adapted from the work of Gardner et al. [33,34]. To control the particle size, water is changed to methanol as a solvent. In 100 mL methanol, 6.1 g of magnesium chloride hexahydrate and 2.41 g of aluminum chloride hexahydrate, with a molar ratio of Mg/Al = 3, are dissolved. This mixture is heated to 65 °C and stirred under reflux. To start the LDH-forming reaction, 3.8 g of sodium hydroxide is dissolved in 100 mL of methanol and added dropwise to the metal salt solution. For a small particle size distribution, the synthesis time from Gardner's work is reduced from 3 days to 1 h. The synthesized product is rigorously washed with methanol to dissolve the by-product NaCl and subsequently dried at 50 °C. The resulting sample is further referred to as HTlc-pure (1) throughout the manuscript.

After allowing the reaction mixture to reach room temperature, it is subjected to centrifugation, and the resulting pellet is dispersed in water. This procedure is repeated until the pH level reaches neutrality. The dispersed material is then left in water overnight to undergo delamination, resulting in a transparent dispersion. This specific form of the delaminated substance is subsequently dried and referred to as HTlc-delaminated (2a). The membrane coating process yields structures with oriented platelets, as seen in the SEM images in part two [1]. To investigate the influence of this orientation, oriented samples are produced by dropping single droplets of the transparent dispersion onto a sample carrier. This process is repeated several times, resulting in platelets that are oriented parallel to the carrier surface. Those samples are further referred to as HTlc-delaminated-oriented (2b).

The delaminated dispersion is subjected to thermal treatment at 400 °C for 3 h in air to activate the agent. Following this treatment, the resulting powder is placed in an evacuated desiccator until the subsequent analysis. This calcined form is labeled as HTlc-calcined (3).

#### 2.1.2. Organo-Silica Matrix

For the synthesis of the matrix material, which enables $CO_2$ separation, the approach is based on the work of Van Gestel [22]. He based the synthesis on pioneering work conducted at the University of Twente in the group of Ten Elshof [20]. The synthesis method used in this work is a simplified version. It involves mixing 16.655 mL of the membrane-forming precursor (BTESE) with 28.14 mL of ethanol (both thermo scientific chemicals), 0.63 mL of nitric acid (65 wt%), and 4.57 mL of water. Respective amounts result in a water-to-hydrolyzable ethoxy group ratio of one. No ice bath is used due to the rapid mixing of the mixture. The resulting mixture is heated to 60 °C and refluxed for 90 min, followed by cooling to room temperature. To stabilize the sol for storage, an additional 50 mL of ethanol is added, and the mixture is stored in the refrigerator (stock sol). To produce the gels, the stock sol was dried at room temperature to produce the lyogel (BTESE-derived lyogel). Additional thermal treatment was carried out at 300 °C for 3 h under an $N_2$ atmosphere to produce the xerogel. This xerogel is further referred to as BTESE-derived xerogel and is also analyzed for comparison.

#### 2.1.3. Mixed-Matrix

To mix the HTlc with the organo-silica, the HTlc must first be converted into an ethanol-based dispersion. Two grams of the calcined and ground Htlc (3) were mixed with 50 mL of ethanol and redispersed using an ultrasonic device for 20 min. Afterward, the dispersion was centrifuged for 20 min at 4000 rpm to remove any undispersed particles. This process was repeated until no undispersed particles were found and a stable dispersion was formed. Then, 5 mL of this sol was mixed with 5 mL of the organo-silica stock-sol and filled up with 40 mL of ethanol. Subsequently, this sol was dried into a powder for analysis. This form is denoted as HTlc-modified organo-silica (4) and the final form for the high-temperature membrane application.

The membrane-forming process and resulting SEM images of the prepared membranes and schematic drawings of the microstructure are given in part 2 of this publication [1].

### *2.2. Analytical Methods*

Structural information is obtained by a combination of infrared (IR) and Raman spectroscopy and X-ray diffraction (XRD). Additionally, its thermal behavior is investigated by thermogravimetric (TGA) experiments.

#### 2.2.1. X-ray Diffraction (XRD)

X-ray diffraction measurements were conducted on an Empyrean diffractometer (Malvern-PANalytical, Almelo, The Netherlands) with a Cu-K$\alpha$ tube operated at 40 mA and 40 kV equipped with a multistrip PIXcel3D detector (255 channels, simultaneously covering 3.347° 2θ) and a Bragg–Brentano HD device. The powder patterns were measured in the range of 5 to 90° 2θ with step size 0.013° 2θ, time per step 1s, slits of 0.125°, soller slits of 2.3°, and sample rotation. The powder patterns were evaluated with HighScorePlus v.5.1 software. The phases were identified using the ICDD (2004) and COD (2021) databases.

Rietveld refinements were performed with TOPAS v.7 for the estimation of the unit cell parameters and the size of coherent scattering domains of hydrotalcite. The structure data of Zhitova et al. [5], ICSD Nr.-133744 and ICSD Nr.-133742 have been used as a starting model.

#### 2.2.2. IR Analysis

IR measurements in Attenuated Total Reflection (ATR) arrangement were performed on powder samples in a Golden Gate ATR cell with a diamond crystal (Specac LTD, Orpington, UK) positioned in a Tensor II spectrometer (Bruker Optics, Ettlingen, Germany) equipped with a deuterated triglycine sulfate (DTGS) detector. Spectra with 64 scans and a spectral resolution of 2 $cm^{-1}$ in the range of 400–4000 $cm^{-1}$ were acquired.

#### 2.2.3. Raman Spectroscopy (RS)

Raman spectroscopic analyses were performed on the powdered samples dusted on glass slides. A WITec alpha300 R equipped with a UHTS300 spectrometer (300 mm focal length) and a Zeiss confocal microscope were employed for single-spot measurements. As an excitation source, a 533 nm laser operated at 50 mW (on sample) was used. The measurements were performed with a 100× objective with a numerical aperture of 0.9 using 600 and 1800 groves/mm holographic gratings with spectral resolution better than 3 $cm^{-1}$ and 1 $cm^{-1}$, respectively. A high-performance back-illuminated CCD camera with 96% quantum efficiency was used for detection. Typical acquisition times were between 5 and 20 s with 5–10 scans. The phase identification was aided by the RRUFF mineral database and an own database integrated into the WITec True Match program. The data processing and preparation of the Raman images were performed with the Project 5.3+ software from WITec (Ulm, Germany). The single spectra were corrected by the cosmic ray removal algorithm, and the consequent subtraction of the background was calculated using the shape algorithm.

#### 2.2.4. Thermal Analysis (TA)

The thermal analyses (TA) were performed on an STA 403 Jupiter F3 (Netzsch, Selb, Germany) equipped with a Pt oven, coupled to a Tensor 27 Fourier transform infrared (FTIR) spectrometer (Bruker-Optics, Ettlingen, Germany). The TA device was purged with $N_2$ (2 × 60 mL/min) and was connected via a transfer gas line to an FTIR gas cell (both kept at 200 °C to prevent condensation), where the detection of the gases released upon heating was performed with a liquid nitrogen cooled MCT (mercury cadmium telluride) detector. The samples were heated at a rate of 10 K/min, and IR spectra of released gases were acquired with 32 scans and spectral resolution of 4 $cm^{-1}$ in the range of 600–4000 $cm^{-1}$. The calibration of the FTIR spectrometer was carried out with certified test gases in the

validity range of Beer–Lambert's law. The quantification of $H_2O$ and $CO_2$ was performed using the method developed by Merz et al. [35].

## 3. Results and Discussion

### *3.1. XRD Results*

Figure 1 shows the X-ray powder patterns of samples 1, 2a, 2b, 3, BTESE, and 4. Table 1 shows refined unit cell parameters considering the 3R and 2H polytypes and calculated sizes of the coherent scattering domains (results from the double Voigt approach) for hydrotalcite in the corresponding samples.

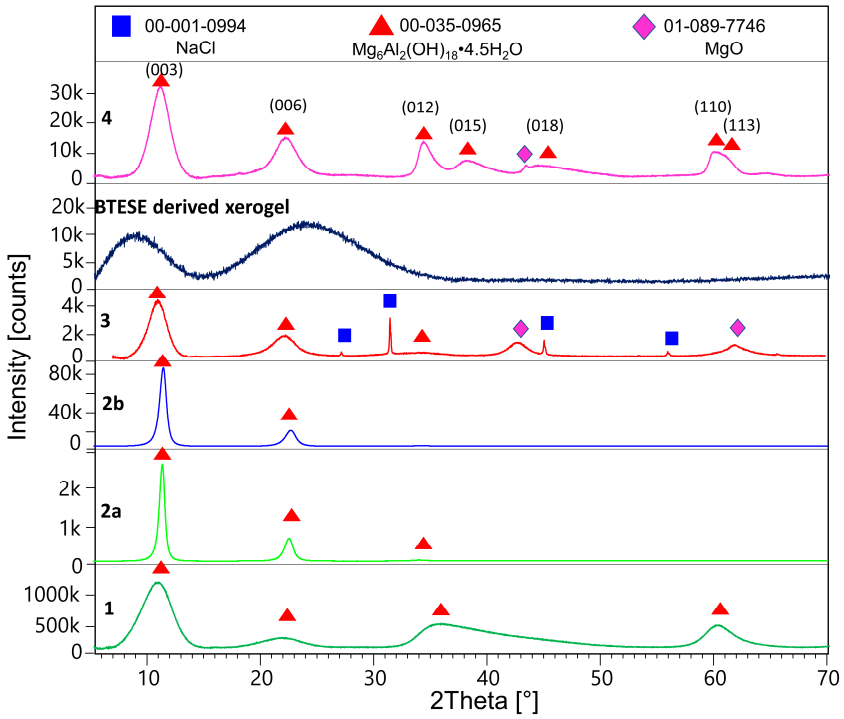



**Figure 1.** Powder XRD patterns of the methanol-washed HTlc-pure sample (1), HTlc-delaminated hydrotalcite (2a), HTlc-oriented sample (2b), HTlc-calcined sample (3), BTESE-derived xerogel, and HTlc-modified organo-silica (4).

**Table 1.** Unit cell parameters and size of the coherent scattering domains of hydrotalcite in samples 1–4 refined for 3R (space group R-3m H) and 2H ($P6_3/mmc$) polytypes.

| **XRD Results** | **Samples** | | | | |
|---|---|---|---|---|---|
| **u.c.p.** | **1** | **2a** | **2b** | **3** | **4** |
| a (Å) | 3.07(1) | 3.066(1) | 3.14(1) | 3.10(5) | 3.064(1) |
| c (Å) 3R | 25.25(1) | 23.683(2) | 23.557(2) | 24.22(1) | 24.25(1) |
| c (Å) 2H | 16.833(7) | 15.788(1) | 15.705(2) | 16.19(1) | 16.181(7) |
| crystal size (nm) | 1.6(1) | 10.6(2) | 8.42(7) | 3.2(1) | 3.4(1) |

After being washed with methanol, the synthesized hydrotalcite HTlc-pure shows very broad reflections pointing to a very small size of the coherent scattering domains of about 1.6 nm (further referred to as crystal size). This confirms the findings of Gardner et al. [32] pointing to a tiny crystal size of hydrotalcite precipitated from methanol solutions of Mg and Al salts. A crystal size of 1.6 nm can also suggest a thickness of one unit cell parameter in the z direction of the 2H polytype consisting of two brucite layers (Table 1). The delaminated and oriented samples (2a and 2b), on the other hand, show very sharp reflections, pointing to crystal sizes of 10.6 and 8.4 nm, respectively. The significantly

higher values for samples 2a and 2b are expected, given the complete hydrolysis of the methoxide ions and the stacking of the hydrotalcite platelets along the [001] direction after drying. The term "delamination" refers to the fact that upon drying, although almost perfect stacking along the z direction of hydrotalcite takes place, a strong disorder in the xy plane is observed. Therefore, only 00l reflections are seen in the patterns of samples 2a and 2b. A tendency for decreasing the size of the *c*-unit cell parameter from 25.2 to 23.68 to 23.56 Å is also observed for samples 1, 2a, and 2b, respectively. This is consistent with the expected exchange of methoxide with $H_2O$. The largest c parameter of sample 1 proves the intercalation of the alkoxide anions between the brucite layers [32]. Samples 2a and 2b show the typical unit cell parameters for $H_2O$ exchanged hydrotalcites (basal spacing of 003 = 7.9Å). The calcined sample (3) once again shows broad reflections of hydrotalcite due to the expected disorder accompanied by additional broad peaks at around 43 and 62 °2Theta, which could be assigned to MgO (ICDD: 01-089-7746). The *c*-unit cell parameter shows a small increase to 24.22 Å. The crystal size decreases to 3.2 nm. Therefore, the calcination at 400 °C leads to partly dehydrated, disordered "hydrotalcite" with similar crystal features as the starting material with disrupted long-range order. In addition, the sample shows some tiny impurities of NaCl, which is a by-product of the synthesis of hydrotalcite. BTESE organo-silica gel shows two broad "humps" at about 8 and 24 °2Theta. The HTlc-modified organo-silica membrane sample (4) shows similar features as sample 3 in its powder pattern but is accompanied by additional 0 kl and 11 l reflections, thus witnessing a random orientation of the "hydrotalcite" platelets which seem to be homogenously distributed in the gel matrix. Considering the crystal size of samples 3 and 4, they consist of four brucite layers.

### *3.2. IR Spectroscopy*

The IR spectra are shown in Figure 2, and relevant bands are summarized in Table 2. Spectrum 1 and 2a are hydrotalcite synthesized and washed with methanol and the delaminated sample, respectively. The assignment is made based on the results of Kloprogge et al. [36] and Frost et al. [37], as well as [38–40]. Sample 1 shows broader bands than 2a and 2b, which is consistent with the XRD results. The main band situated at 1365 $cm^{-1}$ is due to the asymmetrical $\nu_3$ ($CO_3$) mode. The broad high-frequency slope is due to the absorption of $\nu_2$ $CH_3$ bending modes, which are expected in the range of 1440–1480 $cm^{-1}$ [41], and the possible interaction of the $CO_3$ groups of methanol [42]. Additionally, it may witness a large $\Delta\nu_3$ $CO_3$ splitting typical for adsorbed $CO_2$ as monodentate or bidentate carbonate [38]. The corresponding $\nu_2$ ($CO_3$) and $\nu_1$ ($CO_3$) modes are seen at about 870 $cm^{-1}$ and 1075 $cm^{-1}$, respectively. The relatively high intensity of the latter band in the spectrum of sample 1 indicates that this carbonate is due to monodetate and bidentate adsorption of $CO_2$ [38]. It possibly shows contributions of C-O stretching from CO2$CH_3$OH (in the range of 1020–1060 $cm^{-1}$), which is known to be sensitive to interactions with hydrogen bonding [39].

The broad band at 1645 $cm^{-1}$ belongs to the bending vibration of $H_2O$. The broad absorption is possibly due to Mg(Al)-OH interactions. The high-frequency region, 2800–3800 $cm^{-1}$, is marked by a broad band due to $\nu_1$ OH (centered at 3425 $cm^{-1}$) and a very broad low-frequency slope due to $\nu_1$ $CH_3$ and its interaction with OH. Thus, the presence of methoxide anions is once again confirmed.

Samples 2a and 2b show quite similar spectra with bands at 775 $cm^{-1}$ (translation Al-OH) and 860 $cm^{-1}$ ($\nu_2$ $CO_3$). The strongest band is once again the $\nu_3$ $CO_3$ (1365 $cm^{-1}$), lacking the contribution of $CH_3$ bending modes. It may also indicate smaller $\Delta\nu_3$ $CO_3$ splitting due to the presence of polydentate $CO_3$ tightly bonded in the hydrotalcite structure. The band at 1075 $cm^{-1}$ ($\nu_1$ $CO_3$) also lacks the contribution of CO stretching of methanol. The delamination with $H_2O$ also leads to well-pronounced $H_2O$ bands at 1635 $cm^{-1}$ (bending) and 3410 $cm^{-1}$ ($\nu_1$ OH in $H_2O$) with a shoulder at 3610 $cm^{-1}$ ($\nu_1$ OH). The presence of the OH bands at 775 $cm^{-1}$ highlights the difference between sample 1 on one side and samples 2a and 2b on the other side.

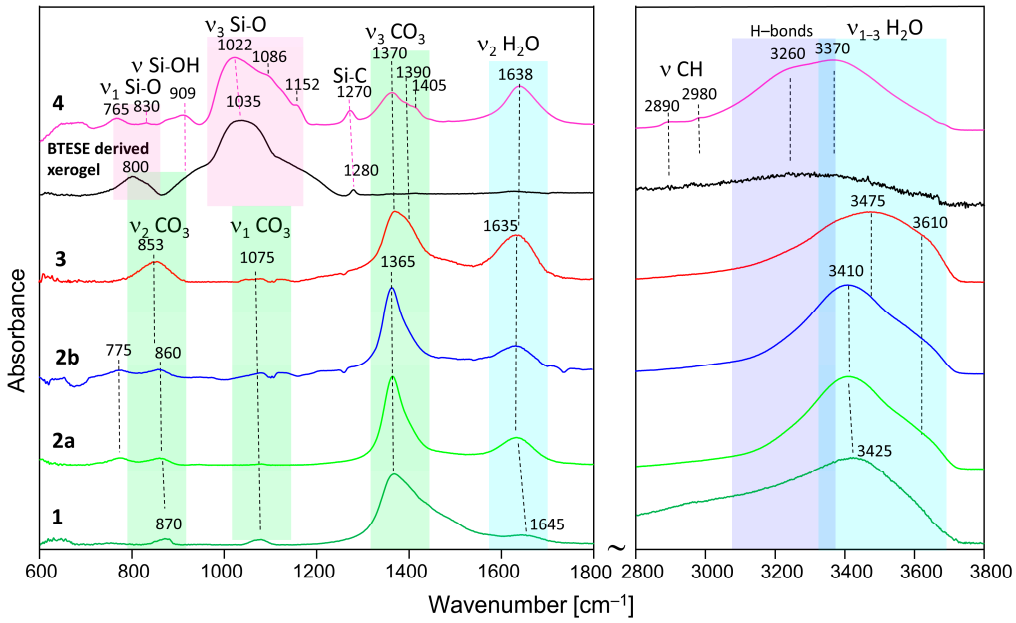



**Figure 2.** ATR-IR spectra of methanol-washed hydrotalcite (HTlc-pure: 1), HTlc-delaminated (2a), HTlc-delaminated-oriented (2b), HTlc-calcined hydrotalcite (3), BTESE-derived xerogel, and HTlc-modified organo-silica (4).

**Table 2.** Band assignment of the IR spectra in Figure 2.

| Hydrotalcite | | | | BTESE, HTlc-Modified Organo-Silica Membrane | | |
|---|---|---|---|---|---|---|
| **Sample** | **1** | **2a,b** | **3** | **Sample** | **BTESE** | **4** |
| **Band Assignment** | **Band Positions ($cm^{-1}$)** | | | **Band Assignment** | **Band Positions ($cm^{-1}$)** | |
| ν Mg(Al)-O | 630 | | | ν Mg(Al)-O | | 650–700 |
| OH libration | | 775 | | OH libration | | 765 |
| $\nu_2$ ($CO_3$) | 870 | 860 | 853 | $\nu_1$ Si-O | 800 | 830 |
| $\nu_1$ ($CO_3$) | 1075 | 1075 | 1075 | Si–OH | 950sh | 909 |
| $\nu_3$ ($CO_3$) | 1365 | 1365 | 1370 | $\nu_3$ Si-O | 1035s | 1022 |
| M,B$\nu_3$ ($CO_3$), $\nu_2$ $CH_3$ | 1400–1500 | | 1390 | $\nu_1$ ($CO_3$) | | 1086 |
| δ $H_2O$ | 1645 | 1635 | 1635 | $\nu_3$ Si-O | 1150sh | 1152 |
| H-bonding | 3000–3400 | 3100–3400 | 3200–3400 | ν Si-C | 1280 | 1270 |
| $\nu_1$ OH($H_2O$) | 3425 | 3420 | 3475 | | $\nu_3$ ($CO_3$) 1370 M,B$\nu_3$ ($CO_3$) 1405 | |
| | | | | δ $H_2O$ | | 1638 |
| | | | | ν-$CH_2$ | | 2890 |
| | | | | ν-$CH_3$ | | 2980 |
| | | | | H-bonding | | 3260 |
| | | | | $\nu_1$ OH($H_2O$ | | 3370 |

M,B$\nu_3$ ($CO_3$)—Monodentate, Bidentate $CO_3$, sh—shoulder, s—strong band.

$H_2O$ interacting with interlayer carbonate in the hydrotalcite structure gives rise to increased absorption between 3000 and 3400 $cm^{-1}$.

The HTlc-calcined sample (3) shows, once again, very broad bands due to increased disorder. The $\nu_2$ bending band of $CO_3$ shows a shift to a lower frequency (853 $cm^{-1}$), whereas the asymmetrical stretching band $\nu_3$ ($CO_3$) shifts to a higher frequency [1370 $cm^{-1}$]. The broader $\nu_3$ $CO_3$ band (with a shoulder at 1390 $cm^{-1}$) may also indicate the presence of different environments of carbonate having on one side polydentate character but

also monodentate and bidentate surface carbonate on the other side. Similar behavior is observed for the OH stretching bands (shift to 3475 $cm^{-1}$), pointing to the presence of more slightly bonded hydroxyls as a result of rehydration.

The IR spectrum of the organo-silica xerogel BTESE is characterized by strong and broad multiple bands in the range of 950–1200 $cm^{-1}$ with a maximum intensity located at about 1035 $cm^{-1}$. These bands could be attributed to asymmetric Si-O stretching modes ($\nu_3$ Si-O) [26] in ring-like siloxane moieties formed via the condensation reaction of silanol groups. Compared to pure $SiO_2$ gels (TEOS, Aerosil), which show frequencies centered at about 1070–1100 $cm^{-1}$ [43], the lower frequency in BTESE could be explained by lower silicate polymerization induced by the presence of organic moieties in the silica network [44,45]. Additionally, it may be due to the lower rate of hydrolysis, as the synthesis was performed with low $H_2O$ content to keep the particle size as low as possible. The band centered around 800 $cm^{-1}$ is characteristic of symmetric Si-O stretching ($\nu_1$ Si-O). A broad absorption seen as a shoulder at about 910 $cm^{-1}$ is ascribed to the stretching vibration of silanol bonds (Si–OH). Its intensity is rather low, which is expected in fired xerogels where enhanced condensation has taken place. The band at 1280 $cm^{-1}$ is characteristic of Si-C stretching vibrations [46]. The range of 2800–3800 $cm^{-1}$ is dominated by broad bands due to $\nu_1$ and $\nu_3$ O-H symmetric and asymmetric stretching of $H_2O$ and OH groups. Due to the firing at 300 °C, a very low intensity of $H_2O$ and OH-related bands is observed. In addition, the low-intensity bands at 2890 and 2980 $cm^{-1}$, typical for C-H stretching vibrations, prove the presence of $CH_2$ and $CH_3$ in the Si–$(CH_2)_2$–Si and (–$OCH_2CH_3$) groups, respectively. The low intensity of the C-H bands marks a high degree of hydrolysis and consequent condensation of silanol groups to siloxanes.

The spectrum of the HTlc-modified organo-silica membrane sample (4) retains similar features characteristic for both BTESE and HTlc-calcined hydrotalcite (3) but with some frequency shifts of the original bands. For example, the organo-silica rings seem to be strongly influenced by the presence of hydrotalcite fragments showing shifts of $\nu_1$ Si-O from 1035 to 1022 $cm^{-1}$ and of Si-C from 1280 to 1270 $cm^{-1}$. The band at 800 $cm^{-1}$ in BTESE is also shifted, pointing to a change in the Si-O-Si bridging angle. The spectrum of sample 4 shows more pronounced silanol groups (909 $cm^{-1}$). The formation of silanol groups correlates with indications for a strong hydrogen-bonded system, which is manifested by a low-frequency shift of the stretching vibrations of $H_2O$ and OH in the spectrum of sample 4 compared to the rest of the samples. The silanol band frequency is higher than that reported by Moriyama et al. for pure BTESE gels (890 $cm^{-1}$) [26]. These observations imply that the interaction between hydrotalcite and BTESE gel most probably takes place via enhanced hydrogen bonding between OH and $H_2O$ of hydrotalcite and Si-O-Si, SiOH, and Si-$CH_2$(3) moieties of BTESE gel. The $CO_3$ modes clearly show the presence of two bands at 1370 and 1405 $cm^{-1}$ with $\Delta\nu_3$ splittings once again higher (35 $cm^{-1}$) than that observed for the calcined sample (20 $cm^{-1}$). It possibly shows an interaction between the surface $CO_3$ groups of hydrotalcite and the xerogel.

### *3.3. Raman Spectroscopy*

The Raman spectra of the 1, 2a, and 2b samples are presented in Figure 3. All samples show bands at 549 $cm^{-1}$ and 457 $cm^{-1}$, characteristic for hydrotalcite, which could be assigned to stretching and bending vibrations (*M*–O, *M*–O–*M*, and O–*M*–O) within the octahedral layers [36]. Most probably, the band at a lower frequency is due to Al-O vibrations, whereas the band at 549 $cm^{-1}$ could be assigned to Mg-O due to the difference in the atomic weight and corresponding quantities. These bands are sharper in samples 2a and 2b. Very pronounced is the band at 1078 $cm^{-1}$ (sample 1) assigned to the symmetrical stretching vibration of $CO_3$ ($\nu_1$ $CO_3$). The corresponding band in samples 1b and 2 is much sharper and shows a frequency shift to 1062 $cm^{-1}$. Additionally, the spectrum of sample 1 shows the presence of bands at 1467 $cm^{-1}$ and 2820 $cm^{-1}$, 2840 $cm^{-1}$, and 2950 $cm^{-1}$ belonging to bending and $\nu_1$ and $\nu_3$ stretching of $CH_3$ groups in methoxide anions [47,48], respectively. Therefore, it is evident that methoxide anions (OR) are grafted to the brucite

layers, partially exchanging OH groups after the formula $[M^{2+}_{(1-x)}\ M^{3+}_{x}\ (OH)_{2-y}]\ (OR)_y]\ A^{n-}_{(x/n)}\ (OR)_y\ .mH_2O$ [32], where $A^{n-}$ represents additional anions like $CO_3^{2-}$, which are inevitably present due to the contact with $CO_2$ from the air.

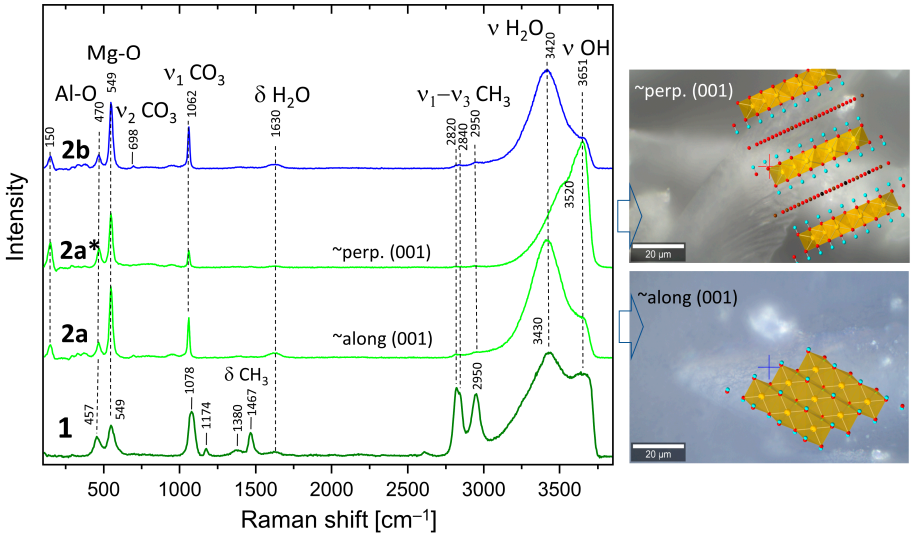



**Figure 3.** Raman spectra of synthesized and washed HTlc-pure sample (1), HTlc-delaminated (2a, 2a*), and HTlc-oriented hydrotalcite (2b). Spectrum 2a of the delaminated sample is taken almost along the [001] direction, thus enhancing the $H_2O$ bending (1630 $cm^{-1}$) and stretching bands (3420 $cm^{-1}$), whereas the spectrum 2a* is measured along the octahedral layers. As a result, the intensity of the OH bands (3651 $cm^{-1}$) is enhanced. The optical images overlaid with the corresponding approximate orientations of the hydrotalcite structure are shown on the right-hand side. Crosses mark the exact positions of the Raman measurements. Completely oriented sample (2b) shows a similar spectrum to 2a (Red dots for oxygen atoms and blue dots for hydrogen atoms).

Low-intensity bands at 1174 and 1380 $cm^{-1}$ are also due to methanol. Broad bands belonging to bending and stretching modes of $H_2O$ and OH groups are present at 1630 $cm^{-1}$ ($\delta$ $H_2O$), 3430 $cm^{-1}$ ($\nu_1/\nu_3$ $H_2O$), and 3650 $cm^{-1}$ ($\nu_3$ OH). Spectra marked as 2a and 2a* are taken in two orientations of the delaminated sample. The former is taken almost along the [001] direction, leading to an enhanced $H_2O$ stretching band (3420 $cm^{-1}$) compared to that taken along the octahedral layers (perpendicular to [001]). Spectrum 2a* shows enhanced intensity of the OH bands (3651 $cm^{-1}$) due to the larger vector components of the OH bonds seen in this direction. The right-hand side of Figure 3 shows optical images overlaid with the corresponding approximate orientations of the hydrotalcite structure. The band at 150 $cm^{-1}$ also shows a higher intensity in the spectrum of sample 2a*, which implies that it may also be due to an OH mode. The opposite trends are observed for both Mg-O modes (549 $cm^{-1}$), $CO_3$ bands ($\nu_1$-$CO_3$), and $\delta$-$H_2O$, which is consistent with the proposed orientation of the crystals. The spectrum of the oriented sample (2b) is strikingly similar to that of 2a, which confirms these considerations once again. There are remarkable differences in the frequencies of Al-O and $CO_3$ bands in the methanol-washed sample (1) and samples 2a and 2b. Whereas the former shifts to higher frequency (470 $cm^{-1}$), the latter shifts to 1062 $cm^{-1}$. Therefore, methanol strongly influences the carbonate groups in the interlayer and possibly selectively the Al from the octahedral layers.

Figure 4 shows a comparison of the Raman spectra of HTlc-calcined hydrotalcite (3), BTESE, and mixed HTlc-modified organo-silica membrane (4). Sample 3 shows broader bands than the delaminated and oriented samples. The frequencies of the octahedral Mg-O vibrations change to a minimally higher frequency (551 $cm^{-1}$), whereas those typical for Al-O shift to the lower (450 $cm^{-1}$). The most intense band of MgO is expected also in this region [49]. Additionally, a broad band occurs centered at about 670 $cm^{-1}$, possibly due to

the partial formation of disordered spinel, which needs to be avoided as it has no relevant $CO_2$ adsorption capacity [50].

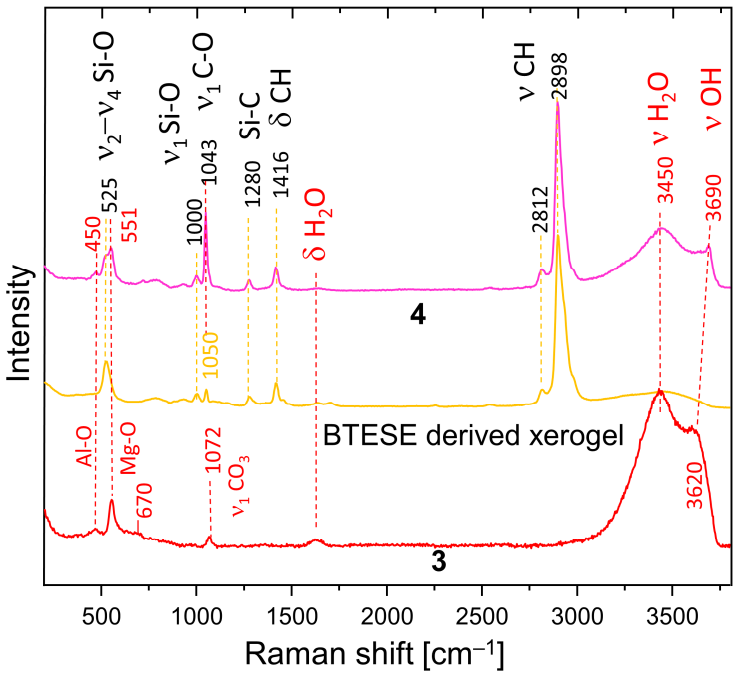



**Figure 4.** Raman spectra of HTlc-calcined sample (3), BTESE xerogel, and HTlc-modified organo-silica (4).

Both are expected products from the breakdown of hydrotalcite [51]. The symmetrical stretching of $CO_3$ is observed at 1072 $cm^{-1}$ instead of 1078 $cm^{-1}$, pointing to a change in the environment of the carbonate anion. In addition, the intensity of this band is considerably lower than in the spectra of not calcined samples (Figure 3). The difference in the vibrational frequencies of the stretching bands of $H_2O$ and OH in the spectrum of the calcinated sample (3450 $cm^{-1}$, 3620 $cm^{-1}$) compared to the spectra of samples 1b and 2 (3420 $cm^{-1}$, 3650 $cm^{-1}$) also witness a change in the interlayer environment. A partial rehydration of the sample from air moisture seems possible.

BTESE shows typical CH stretching bands in the range of 2800–3000 $cm^{-1}$. They consist of a very intense band at 2898 $cm^{-1}$ with high-frequency shoulders at 2930 and 2980 $cm^{-1}$ and a small band at a lower frequency (2812 $cm^{-1}$). A band at 1416 $cm^{-1}$ manifests the corresponding bending vibrations. A question arises about the difference in the intensity of the C-H stretching bands in the IR and Raman spectra. A possible explanation is that the ethoxide groups in the xerogel are oriented to the centers of the siloxane rings. Therefore, a relatively low number of such groups is observed at the surface, thus becoming "invisible" for ATR measurements. Si-C stretching is observed at 1280 $cm^{-1}$. In addition, bands typical for breathing vibrations of siloxane rings appear at 525 $cm^{-1}$. They are at a higher frequency than the four-membered siloxane rings of the gels derived from TEOS (490 $cm^{-1}$) [52]. Broad bands at about 790 $cm^{-1}$ and 925 $cm^{-1}$ are attributed to Si-O-Si and Si-OH vibrations, respectively. At 1000 $cm^{-1}$, ($\nu_1$ Si-O) are present. The assignment of the band at 1050 $cm^{-1}$ is somewhat ambiguous. It is also present in non-fired BTESE gels but with lower intensity (not present). Therefore, it could be due to the C-O stretching mode of ethoxy groups $H_3C$-O-R on one side or to Si-O stretching modes in environments different than siloxanes (Si-O-Si). These might be the (C)Si-O environments typical for the BTESE rings.

The Raman spectrum of the mixture of BTESE and calcined hydrotalcite (4) shows complementary features characteristic for both constituents and, in addition, strong indications of interactions between the two. The band at 1043 $cm^{-1}$ could be due to C-O modes of methanol used as a dispersion medium or ethanol remnants from the synthesis of the

BTESE, but an influence of (C)Si-O, as discussed above, is also possible. The intensity of this band is much higher in spectrum 4 than in spectra 3 and BTESE, respectively.

Therefore, the more probable explanation is that this band is due to adsorbed $CO_2$ as a carbonate, which may be shared between BTESE and calcined hydrotalcite. The small shoulder on the high-frequency side of this band shows the presence of additional environments of $CO_3$ in the sample, also witnessed by the $\Delta\nu_3$ splitting in the IR spectra. A new feature is the pronounced OH band shifted to 3690 $cm^{-1}$. The higher frequency indicates a lower dependence on the environment, which is characteristic of unassociated OH groups on the surface of the mixture. The unchanged frequencies of the Mg-O and Al-O bands give a hint that the interaction between hydrotalcite and BTESE gel takes place over OH and $CO_3$ species characteristic for the interlayer and not over bridging oxygens from the main octahedral layers. Whatever assignment of the band at 1043 $cm^{-1}$ is correct (ethoxy groups or $CO_3$ groups), the observed frequency shift and intensity might be an indication for cross-linking between hydrotalcite and BTESE gel.

### *3.4. Thermal Analysis*

The TGA curves are presented in Figure 5A. Figure 5B,C shows the traces of $CO_2$ and $H_2O$ releases, respectively, as a function of temperature. A comparison between A, B, and C allows the assignment of the observed weight loss. Sample 1 shows an early inflection point (at 70 °C) of the weight loss between 30 and 200 °C probably due to two factors: (1) a large quantity of adsorbed $H_2O$ because of the very high specific area and (2) decomposition of the methoxide anions. Compared to the $H_2O$ exchanged and delaminated sample (2a), the weight loss in the range of 30–250 °C of sample 1 takes place not only earlier but is also higher: 14.7% compared to 12.2%. The latter correlates with the ideal stoichiometry of hydrotalcite, which considers it a loss of absorbed and interlayer $H_2O$. Between 300 and 500 °C, a strong mass loss takes place attributed to almost simultaneous dehydroxylation of the brucite layers and decarbonation of hydrotalcite [53,54]. A comparison of Figure 5B,C for sample 2a allows the interpretation that the $H_2O$ could be separated into two events, one of which precedes the $CO_2$ release marginally.

The observed weight loss between 300 and 500 °C for samples 1 and 2a (27.8% and 26.5%) is way too low compared to the expected theoretical value for full decarbonation and dehydroxylation of hydrotalcite with formula $(Mg_6Al_2(OH)_{16}(CO_3).4H_2O)$: $CO_2$ + $8H_2O$ = 7.3% + 23.9% = 31.2%, based on an M = 604 g/mol. On the other hand, sample 1 is composed of methoxide instead of pure $H_2O$ in the interlayer, and the detected carbonate should only be due to a surface reaction with the $CO_2$ from the air, as shown by the large $\Delta\nu_3$ shift in the IR spectrum. In addition, this carbonate persists at higher temperatures, as observed in [38]. Therefore, the full decomposition of hydrotalcite is reached only at higher temperatures. The small step observed above 900 °C evidences an additional weight loss, especially considering the TG curves of samples 2a and 3. The total mass loss of samples 1 and 2 is 47.1% and 45.3%, respectively, the latter being very close to the theoretical value of 43.1%.

The higher loss of sample 1 is expected, given the large presence of methoxide groups. Calculation of the molar mass considering full substitution of OH by $H_3CO^{1-}$, the presence of $CO_3^{2-}$ and $4H_2O$ (M = 693 g/mol) would result in a total mass loss of 50.4 %, which seems to be exaggerated but explains the higher loss of sample 1. Other authors also reported similar observations [49]. A small contribution to the weight loss above 900 °C could be the melting of residual NaCl, but its content is too low to account for the whole effect. It cannot be ruled out that some Cl is bonded in the hydrotalcite interlayer [55] and references therein].

Sample 3 (HTcl-calcined) shows a total mass loss of 17.2%. It is subdivided into three events taking place between room temperature and 200 °C (6%), 200–400 °C (4.9%), 400–700 °C (2.6%), and 700–1000 °C (3.7%). This shows once again that, on the one hand, the complete decomposition of hydrotalcite takes place at higher temperatures, and on the other hand, particular rehydration and recarbonation take place after calcination.

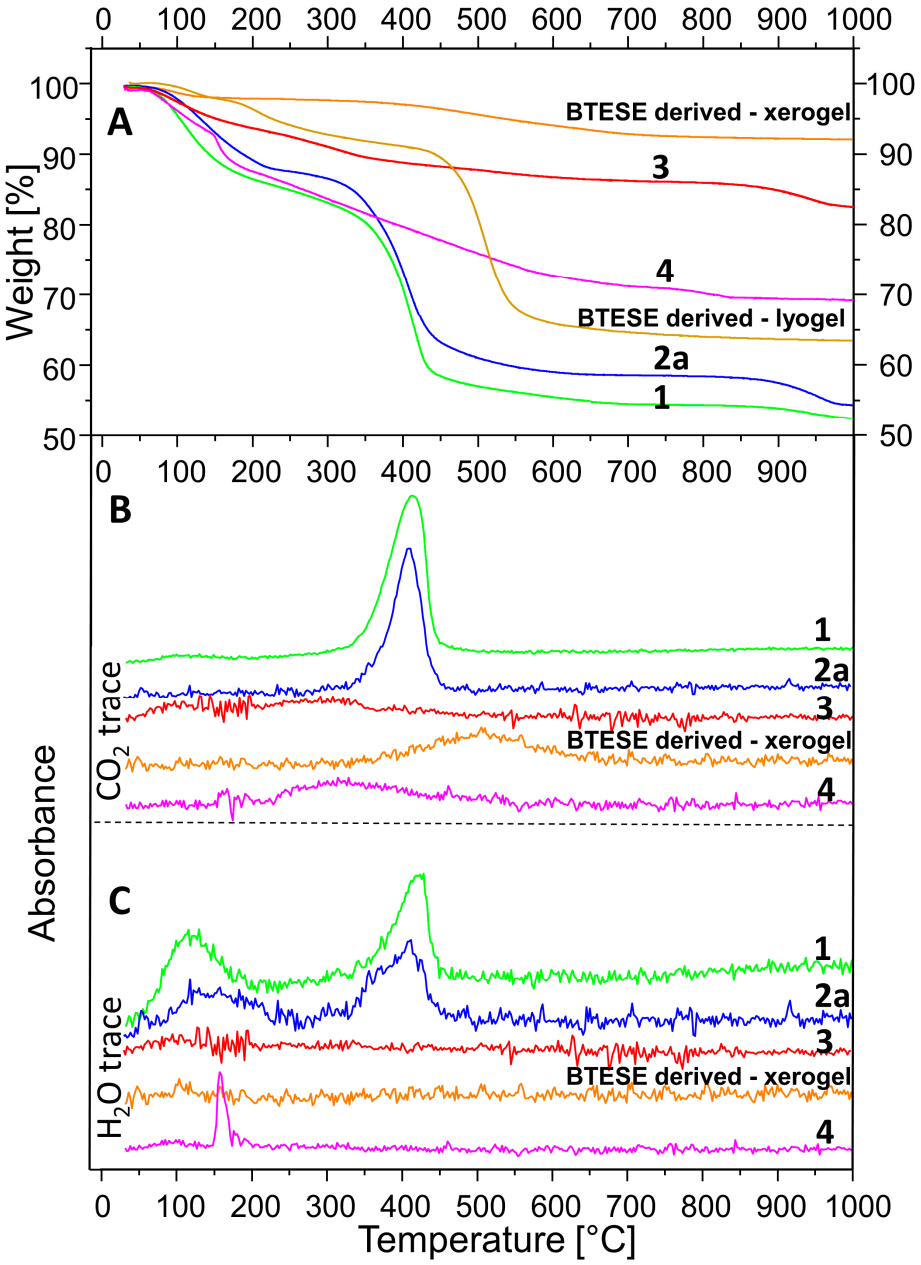



**Figure 5.** TGA coupled with simultaneous FTIR analysis. Thermogravimetric analysis (**A**); $CO_2$ release (**B**); $H_2O$ release (**C**). Samples: HTlc-pure (1); HTlc-delaminated (2a); HTlc-calcined (3), BTESE-derived xerogel; BTESE-derived lyogel, HTlc-modified organo-silica (4).

The thermal behavior of the BTESE-derived xero- and lyogel show a minor weight loss due to adsorbed water below 150 °C. The lyogel, which has not been exposed to temperatures above 50 °C, shows condensation reactions above 200 °C, which results in further water loss. The fired xerogel shows no further condensation reactions. At temperatures above 450 °C, the lyogel undergoes degradation and combustion of ethoxide groups and ethylen bridges with $C_2H_4$, $C_2H_6$, and $C_2H_5OH$ as products [56]. The total weight loss for the lyogel accumulates to 37%.

The continuous weight loss for the BTESE-derived xerogel between 300 and 700 °C could be attributed to non-reacted degradation and combustion of ethoxide groups ($–OCH_2CH_3$) and ethylene bridges ($–CH_2–CH_2–$). In this range, a release of $CO_2$ was detected by the IR spectroscopy (Figure 5B). The total weight loss adds up to 7.6%.

Sample 4, as a combination of (3) and BTESE-derived lyogel, shows a total weight loss of 31%. Up to 150 °C, a 5.3% loss is due to the release of adsorbed $H_2O$ and possibly ethanol. Between 150 and 200 °C, a sharp weight loss of 6.9% is observed, which corresponds to the water loss from the condensation of the Si–OH groups upon the formation of Si–O–Si bonds. In the range of 200–650 °C, a gradual weight loss takes place, which is mostly due to the release of $CO_2$, as seen in Figure 5B. It seems to be a combination of $CO_2$ release from hydrotalcite remnants and combustion of ethoxides, as described above. The sharp loss between 150 and 200 °C is not observable in the TG curves of the "pure" constituents BTESE gel and calcined hydrotalcite. This shows unequivocally that both are not only chemically connected in the mixture but also that this happens via hydrogen bonding between silanol groups and active oxygen centers of the brucite layers on one side and OH groups of the brucite layers and oxygens from the silicate network on the other side following the reaction MgO-H + Si-OH → MgOSi + $H_2O$. Given the basicity of hydrotalcite on the one hand and the variability of the degree of hydrolysis of the BTESE gel in dependence on pH [26] on the other hand, a variable degree of cross-linking both within BTESE siloxane rings and between siloxane rings and brucite layers could be achieved for the design of membranes with different properties.

## 4. Conclusions

This study presents a novel approach for the preparation of mixed-matrix membranes for gas separation consisting of hydrotalcite dispersed in a matrix of an organo-silica gel derived from 1,2-bis(triethoxysilyl)ethane (BTESE). The procedure includes synthesis and subsequent agent-free delamination of hydrotalcite nanoparticles. This is followed by the dispersion of the delaminated and calcined hydrotalcite in the organo-silica gel matrix. The materials were systematically examined after each preparation step by XRD, Raman, IR spectroscopy, and TG analysis. The results show substantial evidence for the successful preparation, delamination, dispersion, and calcination processes. XRD provides valuable information about the layer thickness, unit cell parameters, and size of coherent scattering domains of hydrotalcite after synthesis and every treatment step. The synthesis in methanol produces nano-sized hydrotalcite with an average of two brucite layer thicknesses. The consequent hydrolysis and delamination are proven by the lowering of the c-unit cell parameter and the formation of stacking faults along the z direction. The results from IR and Raman spectroscopy reveal the nature of the bonding mechanisms between hydrotalcite and BTESE-derived gel. These include forming a strong hydrogen bonding system between the interlayer species (OH groups, $CO_3^{2-}$) of hydrotalcite and siloxane oxygens on one hand and silanol active gel centers and bridging oxygens from brucite layers on the other. The interaction between ethoxide groups and hydrotalcite can also not be excluded, but further investigations are necessary to elucidate their role. These findings may give an impetus for further development of mixed-membranes containing inorganic sorption or catalytic agents combined with organo-silica networks. Part 2 of this work will present a study of all the investigated materials for their permeation and separation behavior.

**Author Contributions:** Conceptualization, L.B., K.G., and P.S.; methodology, L.B., K.G., P.S., and D.S.; formal analysis, K.G., A.U., and L.B.; investigation, L.B., K.G., A.U., and P.S.; writing—original draft preparation, K.G. and L.B.; writing—review and editing, K.G., P.S., A.U., and D.S.; supervision, D.S. All authors have read and agreed to the published version of the manuscript.

**Funding:** Program-oriented funding for this research was provided through the German Helmholtz Association in the frame of the "Materials and Technologies for the Energy Transition" program.

**Institutional Review Board Statement:** Not applicable.

**Data Availability Statement:** The data that support the findings of this study are available from the corresponding author upon request.

**Conflicts of Interest:** The authors declare no conflicts of interest.

## References


1. Bünger, L.; Kurtz, T.; Garbev, K.; Stemmermann, P.; Stapf, D. Mixed-Matrix Organo–Silica–Hydrotalcite Membrane for $CO_2$ Separation Part 2: Permeation and Selectivity Study. *Membranes* **2024**, *14*, 156. [CrossRef] [PubMed]
2. Hochstetter, C. Untersuchung über die Zusammensetzung einiger Mineralien. *J. Prakt. Chem.* **1842**, *27*, 375–378. [CrossRef]
3. Mills, S.J.; Christy, A.G.; Schmitt, R.T. The creation of neotypes for hydrotalcite. *Mineral. Mag.* **2016**, *80*, 1023–1029. [CrossRef]
4. Allmann, R.; Jepsen, H.P. Die Struktur des Hydrotalkits. *Neues Jb. Miner. Monat.* **1969**, *1969*, 544–551.
5. Bellotto, M.; Rebours, B.; Clause, O.; Lynch, J.; Bazin, D.; Elkaim, E. A reexamination of hydrotalcite crystal chemistry. *J. Phys. Chem.* **1996**, *100*, 8527–8534. [CrossRef]
6. Zhitova, E.; Krivovichev, S.; Pekov, I.; Greenwell, H. Crystal chemistry of natural layered double hydroxides. 5. Single-crystal structure refinement of hydrotalcite, $[Mg_6Al_2(OH)_{16}](CO_3)(H_2O)_4$. *Mineral. Mag.* **2019**, *83*, 269–280. [CrossRef]
7. Evans, D.G.; Slade, R.C.T. Structural Aspects of Layered Double Hydroxides. In *Layered Double Hydroxides. Structure and Bonding*; Duan, X., Evans, D.G., Eds.; Springer: Berlin/Heidelberg, Germany, 2005; Volume 119. [CrossRef]
8. Ram Reddy, M.K.; Xu, Z.P.; Lu, G.Q.; Diniz da Costa, J.C. Layered Double Hydroxides for $CO_2$ Capture: Structure Evolution and Regeneration. *Ind. Eng. Chem. Res.* **2006**, *45*, 7504–7509. [CrossRef]
9. León, M.; Díaz, E.; Bennici, S.; Vega, A.; Ordóñez, S.; Auroux, A. Adsorption of $CO_2$ on Hydrotalcite-Derived Mixed Oxides: Sorption Mechanisms and Consequences for Adsorption Irreversibility. *Ind. Eng. Chem. Res.* **2010**, *49*, 3663–3671. [CrossRef]
10. Wang, Q.; Tay, H.H.; Ng, D.J.W.; Chen, L.; Liu, Y.; Chang, J.; Zhong, Z.; Luo, J.; Borgna, A. The effect of trivalent cations on the performance of Mg-M-$CO_3$ layered double hydroxides for high-temperature $CO_2$ capture. *Chem. Sus. Chem.* **2010**, *3*, 965–973. [CrossRef] [PubMed]
11. Bublinski, M. CO2-Abtrennung aus Synthesegasen mit Hydrotalciten unter Hochtemperatur-Hochdruckbedingungen. Ph.D. Thesis, University of Stuttgart, Stuttgart, Germany, 2017. [CrossRef]
12. Adachi-Pagano, M.; Forano, C.; Besse, J.-P. Delamination of layered double hydroxides by use of surfactants. *Chem. Commun.* **2000**, *1*, 91–92. [CrossRef]
13. Xie, J.; Khalid, Z.; Oh, J.-M. Recent advances in the synthesis of layered double hydroxides nanosheets. *B. Kor. Chem. Soc.* **2022**, *44*, 100–111. [CrossRef]
14. Shirin, V.A.; Sankar, R.; Johnson, A.P.; Gangadharappa, H.; Pramod, K. Advanced drug delivery applications of layered double hydroxide. *J. Control. Release* **2021**, *330*, 398–426. [CrossRef]
15. Mao, N.; Zhou, C.H.; Tong, D.S.; Yu, W.H.; Lin, C.C. Cynthia Lin, Exfoliation of layered double hydroxide solids into functional nanosheets. *Appl. Clay Sci.* **2017**, *144*, 60–78. [CrossRef]
16. Kim, T.W.; Sahimi, M.; Tsotsis, T.T. The Preparation and Characterization of Hydrotalcite Thin Films. *Ind. Eng. Chem. Res.* **2009**, *48*, 5794–5801. [CrossRef]
17. Fajrina, N.; Yusof, N.; Ismail, A.; Jaafar, J.; Aziz, F.; Salleh, W.; Nordin, N. MgAl-$CO_3$ layered double hydroxide as potential filler in substrate layer of composite membrane for enhanced carbon dioxide separation. *J. Environ. Chem. Eng.* **2021**, *9*, 106164. [CrossRef]
18. Huang, N.; Wang, C.; Chen, C. Ethylene vinyl acetate copolymer/Mg-Al-layered double hydroxide nanocomposite membranes applied in $CO_2/N_2$ gas separation. *Polym. Compos.* **2021**, *42*, 4065–4072. [CrossRef]
19. Wiheeb, A.D.; Shakir, S.W.; Othman, M.R. Synthesis and Characterization of Mesoporous Hydrotalcite-Alumina Membrane for Carbon Dioxide Enrichment. *IOP Conf. Ser. Mater. Sci. Eng.* **2018**, *454*, 12107. [CrossRef]
20. de Vos, R.M.; Verweij, H. High-selectivity, high-flux silica membranes for gas separation. *Science* **1998**, *279*, 1710–1711. [CrossRef]
21. Elshof, J.E.T. Hybrid Materials for Molecular Sieves. In *Handbook of Sol-Gel Science and Technology, Living Reference Work*; Klein, L.C., Aparicio, M., Jitianu, A., Eds.; Springer International Publishing: Cham, Switzerland, 2016; pp. 1–27. [CrossRef]
22. Kanezashi, M.; Matsugasako, R.; Tawarayama, H.; Nagasawa, H.; Tsuru, T. Pore size tuning of sol-gel-derived triethoxysilane (TRIES) membranes for gas separation. *J. Membr. Sci.* **2017**, *524*, 64–72. [CrossRef]
23. Van Gestel, T.; Velterop, F.; Meulenberg, W.A. Meulenberg, Zirconia-supported hybrid organosilica microporous membranes for $CO_2$ separation and pervaporation. *Sep. Purif. Technol.* **2021**, *259*, 118114. [CrossRef]
24. Castricum, H.L.; Kreiter, R.; van Veen, H.M.; Blank, D.H.; Vente, J.F.; Elshof, J.E.T. High-performance hybrid pervaporation membranes with superior hydrothermal and acid stability. *J. Membr. Sci.* **2008**, *324*, 111–118. [CrossRef]
25. Yu, L.; Kanezashi, M.; Nagasawa, H.; Guo, M.; Moriyama, N.; Ito, K.; Tsuru, T. Tailoring Ultramicroporosity To Maximize $CO_2$ Transport within Pyrimidine-Bridged Organosilica Membranes. *ACS Appl. Mater. Interfaces* **2019**, *11*, 7164–7173. [CrossRef]
26. Castricum, H.L.; Paradis, G.G.; Mittelmeijer-Hazeleger, M.C.; Kreiter, R.; Vente, J.F.; Elshof, J.E.T. Tailoring the separation behavior of hybrid organosilica membranes by adjusting the structure of the organic bridging group. *Adv. Funct. Mater.* **2011**, *21*, 2319–2329. [CrossRef]
27. Kanezashi, M.; Yada, K.; Yoshioka, T.; Tsuru, T. Design of silica networks for development of highly permeable hydrogen separation membranes with hydrothermal stability. *J. Am. Chem. Soc.* **2009**, *131*, 414–415. [CrossRef]
28. Moriyama, N.; Nagasawa, H.; Kanezashi, M.; Ito, K.; Tsuru, T. Bis(triethoxysilyl)ethane (BTESE)-derived silica membranes: Pore formation mechanism and gas permeation properties. *J. Sol-Gel Sci. Technol.* **2018**, *86*, 63–72. [CrossRef]

29. Agirre, I.; Arias, P.L.; Castricum, H.L.; Creatore, M.; Elshof, J.E.T.; Paradis, G.G.; Ngamou, P.H.; van Veen, H.M.; Vente, J.F. Hybrid organosilica membranes and processes: Status and outlook. *Sep. Purif. Technol.* **2014**, *121*, 2–12. [CrossRef]
30. Leroux, F.; Adachi-Pagano, M.; Intissar, M.; Chauvière, S.; Forano, C.; Besse, J.-P. Delamination and restacking of layered double hydroxides. *J. Mater. Chem.* **2001**, *11*, 105–112. [CrossRef]
31. Piccinni, M.; Bellani, S.; Bianca, G.; Bonaccorso, F. Nickel-Iron Layered Double Hydroxide Dispersions in Ethanol Stabilized by Acetate Anions. *Inorg. Chem.* **2022**, *61*, 4598–4608. [CrossRef]
32. Othman, M.R.; Helwani, Z.; Martunus; Fernando, W.J.N. Synthetic hydrotalcites from different routes and their application as catalysts and gas adsorbents: A review. *Appl. Organometal. Chem.* **2009**, *23*, 335–346. [CrossRef]
33. Gursky, J.A.; Blough, S.D.; Luna, C.; Gomez, C.; Luevano, A.N.; Gardner, E.A. Gardner, Particle-particle interactions between layered double hydroxide nanoparticles. *J. Am. Chem. Soc.* **2006**, *128*, 8376–8377. [CrossRef]
34. Gardner, E.; Huntoon, K.M.; Pinnavaia, T.J. Direct Synthesis of Alkoxide-Intercalated Derivatives of Hydrocalcite-like Layered Double Hydroxides: Precursors for the Formation of Colloidal Layered Double Hydroxide Suspensions and Transparent Thin Films. *Adv. Mater.* **2001**, *13*, 1263. [CrossRef]
35. Merz, D.; Dregert, O.; Garbev, K.; Stemmermann, P. A reliable quantitative TA-FTIR method for cementitious material characterization. In Proceedings of the GEFTA-STK-Joint Meeting on Thermal Analysis and Calorimetry, Saarbrücken, Germany, 10–12 October 2012; Volume 53.
36. Kloprogge, J.T.; Wharton, D.; Hickey, L.; Frost, R.L. Infrared and Raman study of interlayer anions $CO_3^{2-}$, $NO_3^-$, $SO_4^{2-}$ and $ClO_4^-$ in Mg/Al-hydrotalcite. *Am. Mineral.* **2002**, *87*, 623–629. [CrossRef]
37. Frost, R.L.; Spratt, H.J.; Palmer, S.J. Infrared and near-infrared spectroscopic study of synthetic hydrotalcites with variable divalent/trivalent cationic ratios. *Spectrochim. Acta Part A Mol. Biomol. Spectrosc.* **2009**, *72*, 984–988. [CrossRef]
38. Hernandez-Moreno, M.J.; Ulibarri, M.A.; Rendon, J.L.; Serna, C.J. IR characteristics of hydrotalcite-like compounds. *Phys. Chem. Miner.* **1985**, *12*, 34–38. [CrossRef]
39. Mališová, M.; Horňáček, M.; Mikulec, J.; Hudec, P.; Jorík, V. FTIR study of hydrotalcite. *Acta Chim. Slov.* **2018**, *11*, 147–166. [CrossRef]
40. Coenen, K.; Gallucci, F.; Mezari, B.; Hensen, E.; van Sint Annaland, M. An in-situ IR study on the adsorption of $CO_2$ and $H_2O$ on hydrotalcites. *J. CO2 Util.* **2018**, *24*, 228–239. [CrossRef]
41. Dawes, A.; Mason, N.J.; Fraser, H. Using the C-O stretch to unravel the nature of hydrogen bonding in low-temperature solid methanol-water condensates. *Phys. Chem. Chem. Phys. PCCP* **2016**, *18*, 1245–1257. [CrossRef] [PubMed]
42. Plyler, E.K. Infrared spectra of methanol, ethanol, and n-propanol. *J. Res. Nat. Bur.Stand.* **1952**, *48*, 281–286. [CrossRef]
43. Rosales-Reina, B.; Cruz-Quesada, G.; Padilla-Postigo, N.; Irigoyen-Razquin, M.; Alonso-Martínez, E.; López-Ramón, M.V.; Espinal-Viguri, M.; Garrido, J.J. Tunability of Hybrid Silica Xerogels: Surface Chemistry and Porous Texture Based on the Aromatic Precursor. *Gels* **2023**, *9*, 382. [CrossRef]
44. Kim, Y.-H.; Hwang, M.S.; Kim, H.J.; Kim, J.Y.; Lee, Y. Infrared spectroscopy study of low-dielectric-constant fluorine-incorporated and carbon-incorporated silicon oxide films. *J. Appl. Phys.* **2001**, *90*, 3367–3370. [CrossRef]
45. Meng, L.; Kanezashi, M.; Wang, J.; Tsuru, T. Permeation properties of BTESE–TEOS organosilica membranes and application to $O_2/SO_2$ gas separation. *J. Membr. Sci.* **2015**, *496*, 211–218. [CrossRef]
46. Wahab, M.A.; Kim, I.; Ha, C.-S. Hybrid periodic mesoporous organosilica materials prepared from 1,2-bis (triethoxysilyl) ethane and (3-cyanopropyl) triethoxysilane. *Micropor. Mesopor. Mat.* **2004**, *69*, 19–27. [CrossRef]
47. Keefe, C.D.; Gillis, E.A.L.; MacDonald, L. Improper Hydrogen-Bonding CH Center Dot Y Interactions in Binary Methanol Systems As Studied by FTIR and Raman Spectroscopy. *J. Phys. Chem. A* **2009**, *113*, 2544–2550. [CrossRef] [PubMed]
48. Yu, Y.; Wang, Y.; Lin, K.; Hu, N.; Zhou, X.; Liu, S. Complete Raman spectral assignment of methanol in the C-H stretching region. *J. Phys. Chem. A* **2013**, *117*, 4377–4384. [CrossRef]
49. Ishikawa, K.; Fujima, N.; Komura, H. First—order Raman scattering in MgO microcrystals. *J. Appl. Phys.* **1985**, *57*, 973–975. [CrossRef]
50. Slotznick, S.P.; Shim, S.-H. In situ Raman spectroscopy measurements of $MgAl_2O_4$ spinel up to 1400 °C. *Am. Mineral.* **2008**, *93*, 470–476. [CrossRef]
51. Kloprogge, J.T.; Frost, R.L. Infrared emission spectroscopic study of the thermal transformation of Mg-, Ni- and Co-hydrotalcite catalysts. *Appl. Catal. A* **1999**, *184*, 61–71. [CrossRef]
52. Matsui, K.; Satoh, H.; Kyoto, M. Raman Spectra of Silica Gel Prepared from Triethoxysilane and Tetraethoxysilane by the Sol-Gel Method. *J. Ceram. Soc. Jpn* **1998**, *106*, 528–530. [CrossRef]
53. Kanezaki, E. Effect of atomic ratio Mg/Al in layers of Mg and Al Layered double hydroxide on thermal stability of hydrotalcite-like layered structure by means of in situ high temperature powder X-ray diffraction. *Mat. Res. Bull.* **1998**, *33*, 773–778. [CrossRef]
54. Frost, R.L.; Martens, W.; Ding, Z.; Kloprogge, J.T. DSC and high-resolution TG of synthesized hydrotalcites of Mg and Zn. *J. Therm. Anal. Calorim.* **2003**, *71*, 429–438. [CrossRef]

55. Ke, X.; Bernal, S.A.; Provis, J.L. Uptake of chloride and carbonate by Mg-Al and Ca-Al layered double hydroxides in simulated pore solutions of alkali-activated slag cement. *Cem. Concr. Res.* **2017**, *100*, 1–13. [CrossRef]
56. Kanezashi, M.; Yada, K.; Yoshioka, T.; Tsuru, T. Organic–inorganic hybrid silica membranes with controlled silica network size: Preparation and gas permeation characteristics. *J. Membr. Sci.* **2010**, *348*, 310–318. [CrossRef]

**Disclaimer/Publisher's Note:** The statements, opinions and data contained in all publications are solely those of the individual author(s) and contributor(s) and not of MDPI and/or the editor(s). MDPI and/or the editor(s) disclaim responsibility for any injury to people or property resulting from any ideas, methods, instructions or products referred to in the content.